# Magnetic and transport properties of structural variants of Remeika phases: $Th_3Ir_4Ge_{13}$ and $U_3Ir_4Ge_{13}$

Roman Gumeniuk,[1,2,*] Kristina O. Kvashnina,[3] Walter Schnelle,[1] Andreas Leithe-Jasper,[1] and Yuri Grin[1]

[1]*Max-Planck-Institut für Chemische Physik fester Stoffe, Nöthnitzer Straße 40, 01187 Dresden, Germany*

[2]*Institut für Experimentelle Physik, TU Bergakademie Freiberg, Leipziger Straße 23, 09596 Freiberg, Germany*

[3]*ESRF, 71, Avenue des Martyrs, Grenoble France*

(Received 21 November 2014; revised manuscript received 19 February 2015; published 18 March 2015)

$Th_3Ir_4Ge_{13}$ and $U_3Ir_4Ge_{13}$ crystallize with primitive cubic $Tm_3Co_4Ge_{13}$ and noncentrosymmetric rhombohedral HT-$Y_3Pt_4Ge_{13}$ type of structures, respectively, which are derivatives of the cubic $Yb_3Rh_4Sn_{13}$ prototype. Measurements of magnetic susceptibility, electrical resistivity, specific heat, thermopower, and thermal conductivity reveal that $Th_3Ir_4Ge_{13}$ is a diamagnetic bad metal and undergoes a first-order phase transition at ≈200 K. Charge-density wave (CDW) and structural phase-transition scenarios for $Th_3Ir_4Ge_{13}$ are discussed. $U_3Ir_4Ge_{13}$ is Curie paramagnetic ($\mu_{\text{eff}} = 4.05\ \mu_B$) and orders ferromagnetically at $T_C = 15$ K. For $U_3Ir_4Ge_{13}$ the oxidation state of U is investigated by x-ray absorption spectroscopy. The U $5f$ electrons in this compound are predominantly of itinerant nature.

DOI: 10.1103/PhysRevB.91.094110 PACS number(s): 61.05.cp, 64.70.kd, 75.20.En, 65.40.Ba

## I. INTRODUCTION

The primitive cubic $Yb_3Rh_4Sn_{13}$ type of structure was discovered in the early 1980s by Remeika and co-workers [1]. Its structural arrangement belongs to the group of the so-called cage compounds, where positively charged filler atoms are situated inside large cavities within the covalently bonded atomic framework. Prominent representatives of such structural motif are clathrates and filled skutterudites. The combination of different types of chemical bonding as well as "rattling" effects lead to several exciting physical phenomena making intermetallic cage compounds an object of intensive investigations. More than 100 ternary intermetallic compounds containing fillers like yttrium, alkaline earth ($AE$), rare earth ($RE$), some actinides and frameworks consisting of $d$ elements of subgroups 8–10, as well as such $p$ elements as In, Si, Ge, Sn, and Pb have been shown to crystallize with $Yb_3Rh_4Sn_{13}$ type of structure [2]. In the last few years special attention was paid to the tin-containing compounds $AE_3TM_4Sn_{13}$ ($AE$ = Ca, Sr; $TM$ = Rh, Ir). Being superconductors with $T_c = 7$ and 5 K, $Ca_3Ir_4Sn_{13}$ and $Sr_3Ir_4Sn_{13}$ show a second-order superlattice distortion associated with a charge-density wave (CDW) transition at $T^* = 33$ [3] and 137 K [4], respectively. In both cases, these transitions can be completely suppressed to zero temperature combining chemical and physical pressure leading to a quantum critical point observed in $(Ca_xSr_{1-x})_3Ir_4Sn_{13}$ [5,6]. A recent study also shows that a second-order structural transition at $T^* =$ 138 K in $Sr_3Rh_4Sn_{13}$ (superconductor with $T_c = 5$ K) can be suppressed by applying physical or chemical pressure (e.g., substituting Ca by Sr). This makes the solid solution $(Ca_xSr_{1-x})_3Rh_4Sn_{13}$ an important system for the understanding of the physics underlying structural quantum criticality [7].

A number of publications was also devoted to intermetallic compounds with 3 : 4 : 13 composition containing the actinides Th and U. Such phases are of special interest due to the dual nature of the U $5f$ electronic states, which can be localized or/and itinerant causing unique physical properties. A series of U-containing $U_3M_4Ge_{13}$ ($M$ = Ru, Os, Rh, Ir) compounds crystallizing with primitive cubic $Yb_3Rh_4Sn_{13}$ type was studied in Ref. [8]. $U_3Ru_4Ge_{13}$ was shown to be a Kondo system. No magnetic order was detected for $U_3Os_4Ge_{13}$ down to 4.2 K. In contrast, $U_3Rh_4Ge_{13}$ orders antiferromagnetically at $T_N = 22$ K, while $U_3Ir_4Ge_{13}$ is a ferromagnet with $T_C = 15$–17 K [8]. The powder x-ray diffraction patterns of these compounds show a split of the ($hhh$) reflections corresponding to the $Pm\bar{3}n$ space group and thus do not crystallize with $Yb_3Rh_4Sn_{13}$ type. The compounds $Th_3M_4Sn_{13}$ ($M$ = Ru, Os, Co, Rh, Ir) were studied in Ref. [9]. Superconducting transitions are observed for Ru-, Os-, Rh-, and Ir-containing stannides at 5.7, 5.6, 1.7 [1], and 2.7 K, respectively. $U_3Rh_4Sn_{13}$ is reported to be a magnetically ordered heavy-fermion compound [10]. Recently we successfully prepared compounds showing different variants (cubic $Ca_3Pt_{4+x}Ge_{13-y}$, tetragonal $Yb_3Pt_4Ge_{13}$ [11], rhombohedral HT-$Y_3Pt_4Ge_{13}$ [12], and monoclinic LT-$Y_3Pt_4Ge_{13}$ [13]) of structural distortion of the initial primitive cubic $Yb_3Rh_4Sn_{13}$ prototype, all having interesting physical properties. $U_3Ir_4Ge_{13}$ seems to extend this series of the $Yb_3Rh_4Sn_{13}$ derivatives. Taking into account that almost all 3 : 4 : 13 compounds containing Th are superconductors and looking for an appropriate reference compound to deeper understand the physical properties of $U_3Ir_4Ge_{13}$, we investigated also $Th_3Ir_4Ge_{13}$. In this work we report on the room-temperature crystal structures, and the magnetic, thermal, and transport properties of the $Th_3Ir_4Ge_{13}$ and $U_3Ir_4Ge_{13}$ compounds at low temperatures. In addition, the valence state of U in $U_3Ir_4Ge_{13}$ is investigated by x-ray near edge absorption spectroscopy.

## II. EXPERIMENT

Samples of $Th_3Ir_4Ge_{13}$ and $U_3Ir_4Ge_{13}$ were prepared by arc melting of the metals. Ingots of Th (Goodfellow, 99.5 mass % of metal base and 2 mass % of $ThO_2$), U (Goodfellow, 99.9 mass %), Ir (ChemPur, 99.9 mass %), and Ge (Chempur

*roman.gumeniuk@physik.tu-freiberg.de

 

99.9999 mass %) were used for the syntheses. The resulting pieces were placed in carbon crucibles, sealed in tantalum tubes, and annealed at 900 °C for 7 days. All sample handlings were performed in argon-filled glove boxes [$p(O_2/H_2O) <$ 1 ppm] in a dedicated laboratory with high safety standard at the MPI CPfS [14].

Powder x-ray diffraction (XRD) of the samples was performed on a HUBER G670 imaging plate Guinier camera [Cu$K_{\alpha 1}$ radiation ($\lambda = 1.54056$ Å)]. The *WinXpow* program package [15] was used for phase identification. The lattice parameters and crystal structures were refined by least-squares full-profile fitting of powder XRD data (program package *WinCSD* [16]).

For metallographic investigations a piece of the $Th_3Ir_4Ge_{13}$ sample was examined by energy-dispersive x-ray spectroscopy (EDXS) using a Jeol JSM 6610 scanning electron microscope equipped with an UltraDry EDS detector (ThermoFisher NSS7). The semiquantitative EDXS analyses were performed with 25 keV acceleration voltage and ≈3 nA beam current. The $\phi(\rho z)$ metrics correction model was applied to calculate the $Th_{3.0(3)}Ir_{4.0(3)}Ge_{13.0(3)}$ composition from the intensities of Th$M$, Ir$L$, and Ge$K$ lines.

The x-ray absorption near edge structure (XANES) measurements were performed at beam line ID26 of the European Synchrotron Radiation Facility (ESRF) in Grenoble [17]. The incident energy was selected using the ⟨111⟩ reflection from a double Si crystal monochromator. Rejection of higher harmonics was achieved by three Si mirrors at an angle of 3.5 mrad relative to the incident beam. XANES spectra were measured in high energy resolution fluorescence detection (HERFD) mode using an x-ray emission spectrometer [18]. The U HERFD spectra at the $M_4$ edge were obtained by recording the intensity of the U $M\beta$ emission line (3336.0 eV) as function of the incident energy. The emission energy was selected using the ⟨220⟩ reflection of five spherically bent Si crystal analyzers (with 1 m bending radius) aligned at 75° Bragg angle. The paths of the incident and emitted x rays through air were minimized in order to avoid losses in intensity due to absorption. A combined (incident convoluted with emitted) energy resolution of 0.7 eV was obtained as determined by measuring the full width at half maximum (FWHM) of the elastic peak.

The magnetization was measured (MPMS XL-7, Quantum Design) in external fields between $\mu_0 H = 2$ mT and 7 T and temperatures of 1.8–400 K. The electrical resistivity and the heat capacity were studied down to 0.4 K (PPMS, Quantum Design) using an ac resistivity bridge (LR-700, Linear Research) and the HC option of the PPMS, respectively. Electrical contacts were made with silver-filled epoxy. The Seebeck coefficient and the thermal conductivity were determined simultaneously on the TTO option of a PPMS.

The electronic structures of $Th_3Ir_4Ge_{13}$ and $U_3Ir_4Ge_{13}$ were calculated within the local-density (LDA) and local spin-density (LSDA + $U$, $U = 2$ eV) approximations of the density-functional theory (DFT) using the full-potential FPLO code (version 9.01-35) [19] with the basis set of local orbitals. In scalar relativistic calculations the exchange-correlation potential by Perdew and Wang [20] was used. The $k$ mesh included 120 points in the irreducible part of the first Brillouin zone for both compounds.

## III. RESULTS AND DISCUSSION

### A. Crystal structure

All peaks (besides the weak reflections of $ThO_2$ and free Ge as impurity phases, which were excluded from the refinement) in the powder XRD pattern of $Th_3Ir_4Ge_{13}$ [Fig. 1(a)] were indexed in a primitive cubic lattice with the unit cell parameter $a = 9.0586(3)$ Å. No broadening or atypical asymmetry of the reflections was observed. The FWHM slightly increases with increasing $2\theta$ values varying within the range of 0.10°−0.15° [inset to Fig. 1(a)]. Reflections ($hhl$), in the performed indexing, fulfill extinction conditions $l = 2n$, which suggests space group (SG) $Pm\bar{3}n$ for the crystal structure of $Th_3Ir_4Ge_{13}$. The structure of the $Yb_3Rh_4Sn_{13}$ prototype [1] was chosen as the starting model for the refinement. The final values of the reliability factors were $R_I = 0.093$ and $R_P = 0.131$.

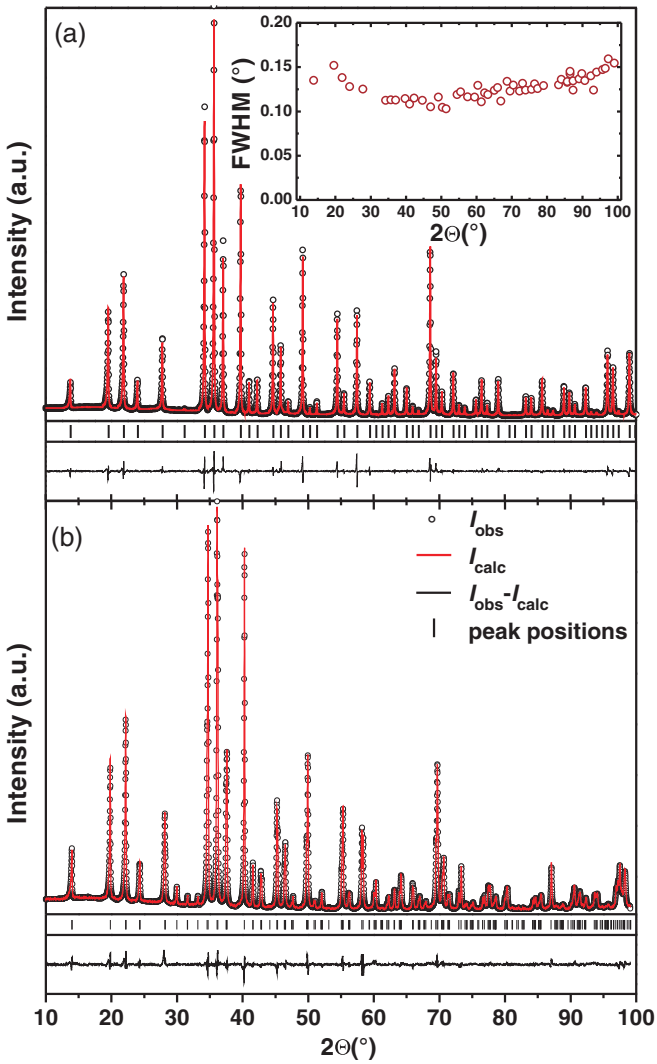


FIG. 1. (Color online) X-ray powder diffraction patterns of $Th_3Ir_4Ge_{13}$ [(a) structure type $Tm_3Co_4Ge_{13}$] and $U_3Ir_4Ge_{13}$ [(b) structure type HT-$Y_3Pt_4Ge_{13}$]. Experimental intensities are shown as circles (black), calculated ones as lines (red, upper part of each panel), and the differences are given as lines (black) in the bottom parts of each panel. The inset shows the observed angular dependence of the full widths of half maximum (FWHM).

TABLE I. Crystallographic data for $Th_3Ir_4Ge_{13}$ [two different structure types, SG $Pm\bar{3}n$; $a = 9.0586(3)$ Å; $R_I = 0.058$, $R_P = 0.091$ ($Tm_3Co_4Ge_{13}$ type)] and $U_3Ir_4Ge_{13}$ [SG $R3c$; $a = 12.6329(1)$ Å, $c = 15.5505(1)$ Å; $R_I = 0.049$, $R_P = 0.070$].

| Atom | Site | $x$ | $y$ | $z$ | $B_{iso}$/Å$^2$ | CN |
|---|---|---|---|---|---|---|
| | | | $Th_3Ir_4Ge_{13}$ ($Yb_3Rh_4Sn_{13}$ type) | | | |
| Th | 6*c* | 1/4 | 0 | 1/2 | 1.36(2) | 16 |
| Ir | 8*e* | 1/4 | 1/4 | 1/4 | 0.91(2) | 9 |
| Ge1 | 2*a* | 0 | 0 | 0 | 0.14(7) | 12 |
| Ge2 | 24*k* | 0 | 0.1442(2) | 0.3064(2) | 4.18(4) | 14 |
| | | | $Th_3Ir_4Ge_{13}$ ($Tm_3Co_4Ge_{13}$ type) | | | |
| Th | 6*c* | 1/4 | 0 | 1/2 | 1.36(2) | 16 |
| Ir | 8*e* | 1/4 | 1/4 | 1/4 | 1.22(1) | 9 |
| Ge1 | 2*a* | 0 | 0 | 0 | 2.04(1) | 12 |
| $Ge2_1$[a] | 24*k* | 0 | 0.1288(3) | 0.2483(3) | 1.45(4) | 14 |
| $Ge2_2$[b] | 24*k* | 0 | 0.1528(2) | 0.3336(2) | 0.91(3) | 14 |
| | | | $U_3Ir_4Ge_{13}$ (HT-$Y_3Pt_4Ge_{13}$ type) | | | |
| U | 18*b* | 0.0012(1) | 0.2505(1) | 0.0000(1) | 1.14(4) | 16 |
| Ir1 | 6*a* | 0 | 0 | 0.0033(1) | 0.75(2) | 9 |
| Ir2 | 18*b* | 0.3318(1) | 0.1656(1) | 0.1690(1) | 1.01(1) | 9 |
| Ge1 | 6*a* | 0 | 0 | 0.2564(2) | 1.16(2) | 12 |
| Ge2 | 18*b* | 0.1751(2) | 0.0073(2) | 0.4170(1) | 1.06(3) | 11 |
| Ge3 | 18*b* | 0.1434(2) | 0.1537(2) | 0.1072(1) | 1.30(3) | 11 |
| Ge4 | 18*b* | 0.0599(2) | 0.2825(2) | 0.1914(1) | 1.54(3) | 12 |
| Ge5 | 18*b* | 0.2086(1) | 0.1649(2) | 0.2959(1) | 1.50(2) | 13 |

[a]Split position $G = 0.36(1)$.
[b]Split position $G = 0.64(1)$.

The corresponding values of the atomic coordinates and displacement parameters are given in Table I.

The refined model is characterized by high $R$ factors, unphysically large displacement parameter for the Ge2 atom, and—as usually observed for these structural arrangements [1]—an enlarged Ge1-Ge2 distance of 3.07(1) Å. Taking into account that no visible signs of a possible symmetry reduction were observed in the XRD pattern of $Th_3Ir_4Ge_{13}$ and to resolve the situation with the displacement parameter for the Ge2 atom, the split of the crystallographic 24*k* position was performed, assuming the coordinate $x \neq 0$ (Wyckoff site 48*l* for Ge2 with occupancy 0.5). However, this operation did not lead to changes of the $R$ factors, $B_{iso}$ for Ge2 as well as the Ge1-Ge2 distance.

In the next step of the refinement a split of the Ge2 position in the (100) plane was undertaken by the introduction of an additional $Ge2_2$ atom occupying the 24*k* crystallographic site. This led to a significant reduction of the $R$ factors and to more realistic displacement parameters of Ge atoms. The final values of $R_I = 0.058$ and $R_P = 0.091$ were obtained. The corresponding calculated XRD pattern is given in Fig. 1(a) and the atomic parameters are listed in Table I.

The obtained structural model is presented in Fig. 2. It indicates the same basic motif as observed for the $Yb_3Rh_4Sn_{13}$ type (Fig. 5 in Ref. [11]), with the only difference that in $Th_3Ir_4Ge_{13}$ the vertices of the icosahedra, trigonal prisms, and the $Sn_4$-like rectangles (marked by blue color) are now "doubled" due to the split of Wyckoff site occupied by Ge. In such a structural arrangement the $Ge2_1$-$Ge2_2$ distance is 0.802(3) Å, while the Ge1-$Ge2_1$ and Ge1-$Ge2_2$ contacts become now 2.534(3) and 3.324(1) Å. The shortening of one of the contacts between the icosahedron centering atom (Ge1) and its vertices ($Ge2_1$) is in agreement with theoretical calculations for different modifications of $Ca_3Pt_{4+x}Ge_{13-y}$ and $Y_3Pt_4Ge_{13}$, which predict structures with shorter Ge-Ge contacts within the icosahedra to be energetically beneficial, due to the separation of Ge 4*p* states into bonding and antibonding states [11,13].

Interestingly, the crystal structure of $Tm_3Co_4Ge_{13}$ [21] adopts the same split of the Ge position, as found here for $Th_3Ir_4Ge_{13}$. In Ref. [21] this has been discussed as a hint to a commensurately modulated structural model with zero modulation vector. Further refinement of the crystal structure of $Tm_3Co_4Ge_{13}$ from powder XRD data assuming super SG $P\bar{4}3n(000)$ led to a completely ordered model and a reduction of the reliability factor $R_I$ from 7.4% to 4.3%, as well as to the bonding character of Ge1-Ge2 contacts within the icosahedra. Our attempts to use the same commensurately modulated structural model in the case of $Th_3Ir_4Ge_{13}$ failed. A refinement resulted in slightly larger $R_I = 0.065$ (instead of 0.058 for the disordered structure) and in an ordered model. However, it was characterized by long Ge1-Ge2 distances of 3.2 Å, thus indicating almost no bonding, in contradiction with theoretical studies (see Sec. III G).

The strongest peaks in the powder XRD pattern of $U_3Ir_4Ge_{13}$ can be indexed using a cubic primitive lattice with $a_{cub} \approx 9$ Å. However, a clear split of (*hhh*) reflections into two with intensity ratio 1 : 2, of (*hll*) into three reflections, as well as single (*h*00) peaks is observed. Such splitting pattern was recently found for rhombohedral HT-$Y_3Pt_4Ge_{13}$. [12] Selected ranges of powder XRD patterns of HT-$Y_3Pt_4Ge_{13}$ and of $U_3Ir_4Ge_{13}$ together with the refined profiles in the rhombohedral SG $R3c$ and possible indexing in the cubic $Pm\bar{3}n$ and rhombohedral $R3c$ SGs are shown in Fig. 3. The structural model of the HT-$Y_3Pt_4Ge_{13}$ type was taken

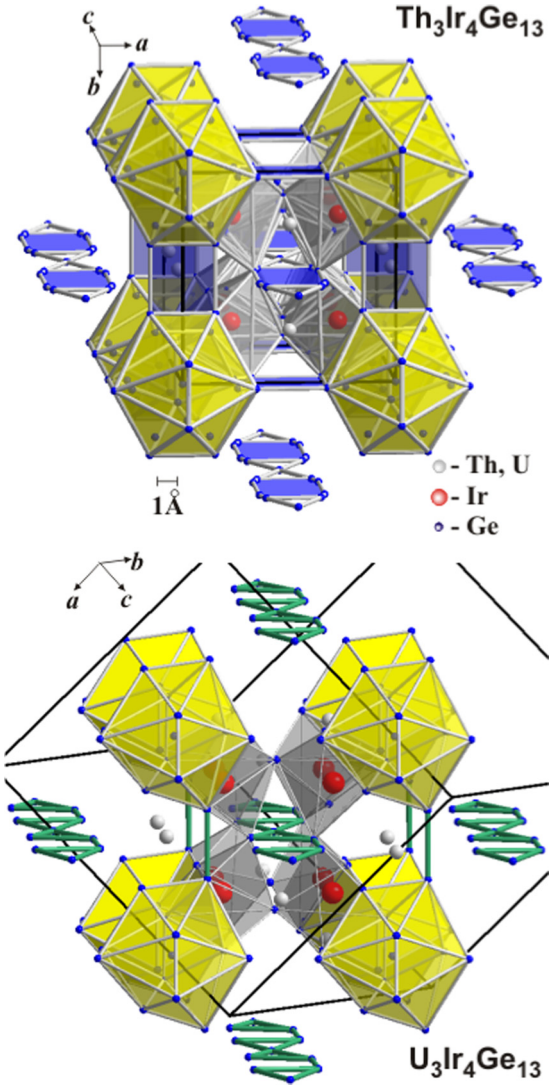


FIG. 2. (Color online) Structural units in the crystal structures of $Th_3Ir_4Ge_{13}$ and $U_3Ir_4Ge_{13}$: distorted icosahedra $Ge1Ge_{24}$ and $Ge1Ge_{12}$ (yellow), distorted trigonal prisms $IrGe_{12}$ and $IrGe_6$ (light gray), as well as distorted $Ge_8$ rectangles (blue, observed only in cubic $Th_3Ir_4Ge_{13}$) and broken quadrangle $Ge_4$ (green, for $U_3Ir_4Ge_{13}$).

for the further refinement of the structure of $U_3Ir_4Ge_{13}$. Crystallographic data, final values of the atomic coordinates, and displacement parameters are presented in Table I; the refined profile is shown in Fig. 1(b).

The obtained rhombohedral unit cell parameters for $U_3Ir_4Ge_{13}$ are related to the initial cubic ones as following: $a_{rhom} = b_{rhom} \approx a_{cub}\sqrt{2}$, $c_{rhom} \approx a_{cub}\sqrt{3}$, which corroborates the close relationship of the atomic arrangement of $U_3Ir_4Ge_{13}$ and of the cubic $Yb_3Rh_4Sn_{13}$ prototype. Indeed, both structures show the same structural motif (cf. Figs. 2 and 5 in Ref. [11]). The only difference is that in the cubic prototype icosahaedra and trigonal prisms are regular, while in the derivative $U_3Ir_4Ge_{13}$ structure they are distorted. It should be noted that interatomic distances in the *p*-element networks are very different in the two types. In Fig. 2 the interatomic contacts which do not exceed the sum of atomic radii of elements ($d_{(Ge\text{-}Ge)} = 2.46$ Å [22]) multiplied by $\sqrt{2}$ are marked by lines.

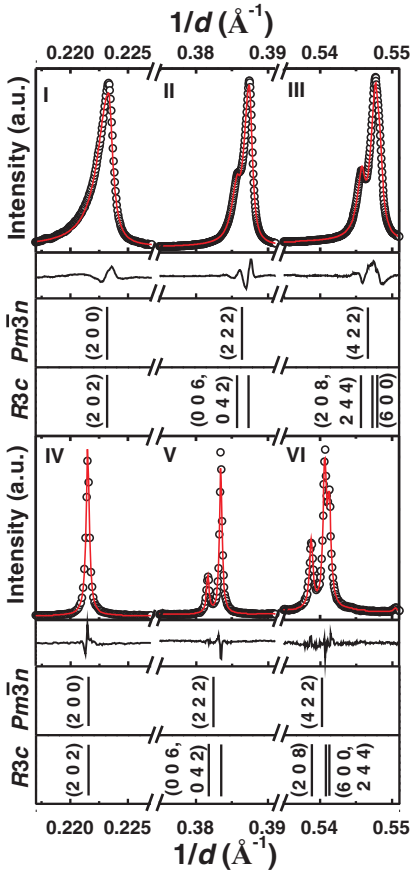


FIG. 3. (Color online) Selected ranges of powder XRD patterns of $U_3Ir_4Ge_{13}$ (top) and HT-$Y_3Pt_4Ge_{13}$ (bottom). Indexes of the reflections in different models are shown in the bottom part of each panel.

In $U_3Ir_4Ge_{13}$ some Ge-Ge contacts exceed this limit, which leads to the disappearance of $Sn_4$-like rectangles (Fig. 5 in Ref. [11]) as observed in the $Yb_3Rh_4Sn_{13}$ prototype and also to the reduction of the coordination number (CN) of some Ge atoms (Table I).

Other interatomic distances in the structures of $Th_3Ir_4Ge_{13}$ and $U_3Ir_4Ge_{13}$ are in most cases in agreement with the sums of atomic radii of the constituents [22]. There are no Ir-Ir contacts, as it is similarly observed in cubic $Yb_3Rh_4Sn_{13}$ prototype. Th-Ge, U-Ge, and Ge-Ge distances are slightly larger than the sums of corresponding radii. The shortest contacts are Ir-Ge, where shrinking by 2.8% and 4.3% was observed for $Th_3Ir_4Ge_{13}$ and $U_3Ir_4Ge_{13}$, respectively.

### B. X-ray absorption spectroscopy

XANES (HERFD) at the U $M_4$ edge is a method to directly probe the U $5f$ shell and thus the valence state of uranium species [23]. In Fig. 4 experimentally obtained HERFD spectra of $U_3Ir_4Ge_{13}$ and $UO_2$ are shown. They are very similar and show almost the same features with the only difference that the spectrum of $U_3Ir_4Ge_{13}$ (i) is characterized by the absence of two high energy features (marked by [green] asterisks) appearing in oxide due to the U-O bonding, (ii) slightly shifted towards lower energies (i.e., 0.2 eV), (iii) a

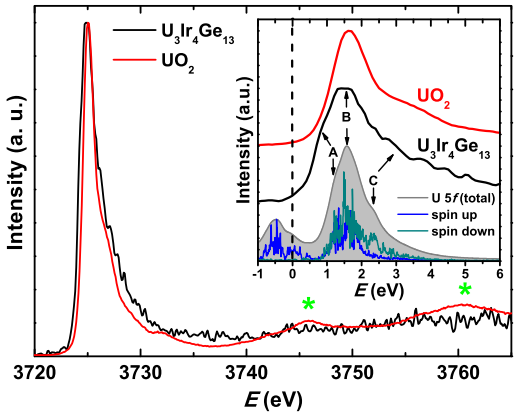


FIG. 4. (Color online) HERFD XANES spectra at the U $M_4$ edge for $U_3Ir_4Ge_{13}$ and $UO_2$. The green asterisks indicate high energy features observed only for uranium (+4) oxide. Inset: Theoretically calculated U $5f$ partial DOS of $U_3Ir_4Ge_{13}$ in comparison with experimentally obtained spectra. The dashed line indicates the Fermi level $E_F$.

bit broadened, and (iv) shows an additional feature A (inset to Fig. 4), which is not so clearly visible in the spectrum of $UO_2$. Since the main feature B is found at almost the same energy position and has also a similar FWHM in both spectra, an oxidation state +4 for the U atoms in $U_3Ir_4Ge_{13}$ could be anticipated. In particular we noted that the energy shift depends on the screening of the core hole by conduction electrons. This effect leads to the shift of the U $L_{III}$ XAS spectrum of $UPd_3$ by ∼1.5 eV in comparison to $UO_2$ despite that both of them were formally understood as U $5f^2$ systems [24]. Therefore, the determination of the oxidation state of uranium in $U_3Ir_4Ge_{13}$ requires further investigations. Taking into account all differences between both spectra the presence of $UO_2$ on the $U_3Ir_4Ge_{13}$ sample surface is rather unlikely. However, additional studies devoted to the issue of possible surface contamination are necessary to draw final conclusions.

The contribution of U $5f$ electrons to the electronic DOS is shown in the inset to Fig. 4. The indicated Fermi level $E_F$ separates the occupied and unoccupied states. The experimentally measured spectra of $U_3Ir_4Ge_{13}$ and $UO_2$ were shifted to coincide with the maximum of U $5f$ partial density of states (DOS, feature B). All main spectral features in the HERFD of $U_3Ir_4Ge_{13}$ are roughly reproduced with the U $5f$ description in FPLO. The only difference is that the experimental spectrum is somewhat broader than the theoretically calculated one. Interestingly, feature C is mostly due to the U $5f$ contributions of one channel ("spin down") in the spin-resolved DOS.

### C. Magnetic susceptibility

$Th_3Ir_4Ge_{13}$ is diamagnetic in the whole studied temperature range with a molar susceptibility $\chi_0 = -400 \times 10^{-6}$ emu mol$^{-1}$ [Fig. 5(a)]. A small step in the susceptibility observed at $T_k^{mag} = 210$ K could indicate a first-order structural phase transition, the formation of a CDW or other opening of a gap at the Fermi surface. Taking into account that both magnetic susceptibility and specific heat are proportional to the DOS at $E_F$, the Sommerfeld-Wilson ratio [25] was used to

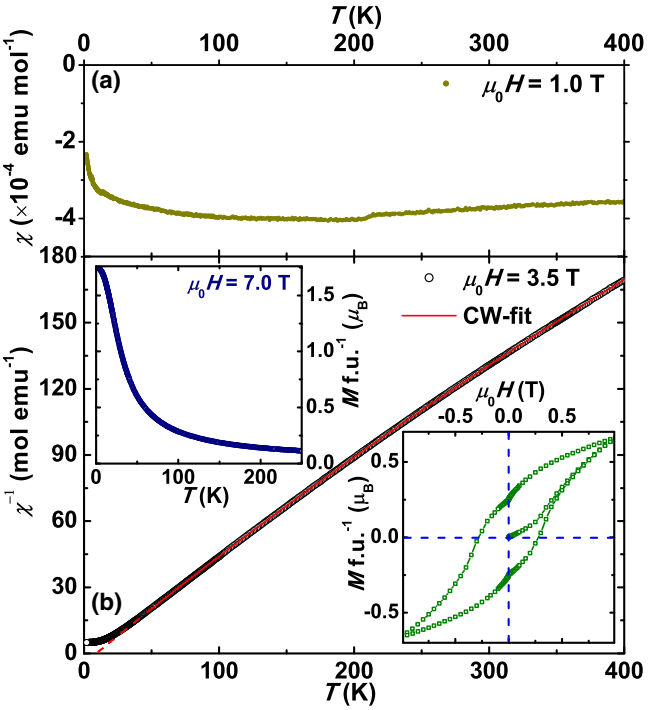


FIG. 5. (Color online) (a) Magnetic susceptibility of $Th_3Ir_4Ge_{13}$ vs temperature. (b) Inverse magnetic susceptibility of $U_3Ir_4Ge_{13}$ together with Curie-Weiss fit. Left inset: Temperature dependence of magnetization. Right inset: Hysteresis loop for fields up to $\mu_0 H = \pm 1$ T at $T = 1.8$ K.

estimate the reduction of DOS corresponding to the gapping at $T_k^{mag}$. The jump $|\Delta\chi_0|$ at the transition temperature is $15 \times 10^{-6}$ emu mol$^{-1}$. Assuming the Sommerfeld-Wilson ratio for free electrons, one obtains $\Delta\gamma_0 = \Delta\chi_0 R_0$, where $R_0 = \pi^2 k_B^2/\mu_B\sqrt{3}$. Hence, $\Delta\gamma_0 = 1$ mJ mol$^{-1}$ K$^{-2}$, which corresponds to the reduction of DOS at $T_k^{mag}$ by only ∼0.4 states eV$^{-1}$ f.u.$^{-1}$. Here it has to be emphasized that the jump $|\Delta\chi_0|$ in the magnetic susceptibility of $Th_3Ir_4Ge_{13}$ is of the same order of magnitude as observed in the $LaPt_2Si_2$ CDW system [26] and one order of magnitude smaller than reported for the $Sr_3Ir_4Sn_{13}$ system (second-order superlattice distortion) [5].

The inverse magnetic susceptibility of $U_3Ir_4Ge_{13}$ is shown in Fig. 5(b). It is described by a modified Curie-Weiss law down to 50 K. An effective magnetic moment $\mu_{eff} = 4.19\ \mu_B$ f.u.$^{-1}$, the Weiss temperature $\theta_P = 4.3$ K and $\chi_0 = +620 \times 10^{-6}$ emu mol$^{-1}$ are determined from a nonlinear fit to $\chi$. $U_3Ir_4Ge_{13}$ orders ferromagnetically at $T_C = 15$ K [left inset Fig. 5(b)], in good agreement with data reported in [8]. The magnetization per formula unit [left inset Fig. 5(b)] reaches about 1.76 $\mu_B$ f.u.$^{-1}$ at 1.8 K in the highest external field of our magnetometer (7 T). A minor hysteresis loop for fields up to $\mu_0 H = \pm 1$ T at $T = 1.8$ K is shown in Fig. 5(b) (right inset). The coercive field at this temperature is about 0.3 T.

### D. Electrical resistivity

The electrical resistivity $\rho$ vs $T$ for $Th_3Ir_4Ge_{13}$ is given in Fig. 6(a). In the temperature range up to 160 K in cooling mode and up to 180 K in warming regime it increases with

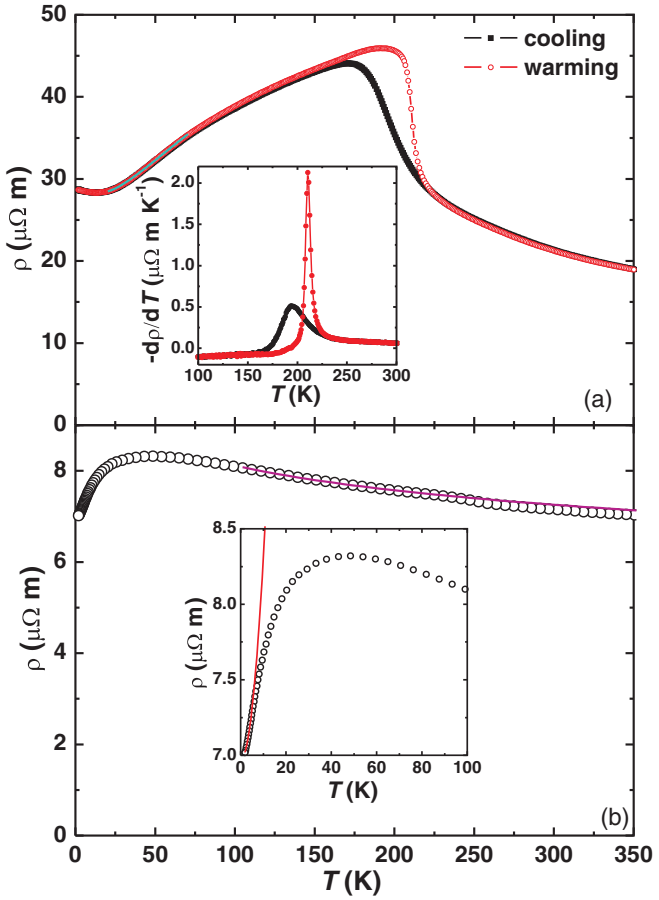


FIG. 6. (Color online) (a) Electrical resistivity $\rho$ vs $T$ for $Th_3Ir_4Ge_{13}$ together with the fit to the Bloch-Grüneisen formula (cyan line) for $20 < T < 70$ K. Inset: $d\rho/dT$ of $Th_3Ir_4Ge_{13}$ vs temperature for cooling and warming modes. (b) Electrical resistivity $\rho$ vs $T$ for $U_3Ir_4Ge_{13}$ with a fit (magenta line) to $\rho_0 + c\ln T$ [$\rho_0 = 11.17(3)$ $\mu\Omega$ m and $c = 0.78(5)$] for $100 < T < 220$ K. Inset: Low temperature resistivity together with a fit to the $\rho_0 + A_{FL}T^2$ formula (red line) for $1.9 < T < 4.5$ K.

increasing temperature. In the range $20 < T < 70$ K $\rho(T)$ is fitted well by the Bloch-Grüneisen equation (1),

$$\rho(T) = \rho_0 + A\left(\frac{T}{\Theta_D}\right)^5 \int_0^{\Theta_R/T} \frac{x^5}{(e^x - 1)(1 - e^{-x})} dx, \quad (1)$$

which indicates simple metallic resistance behavior due to the scattering of electrons by phonons [27]. The fit parameters are the residual resistivity due to defect scattering $\rho_0 = 28.15$ $\mu\Omega$ m; the coefficient depending on the phonon contribution $A = 0.133$ $\mu\Omega$ m, and the Debye temperature $\Theta_D = 153$ K. The low value of $\Theta_D$ obtained here in comparison with that from specific heat is explained by the fact that the former takes into account only longitudinal phonons [28].

Further increase of temperature leads to a sharp drop of the resistivity of $Th_3Ir_4Ge_{13}$ and appearance of a hysteresis while measuring in cooling and warming. The temperatures $T_k^{warm} = 211$ K and $T_k^{cool} = 194$ K are defined as maxima in $-d\rho/dT$ [inset to Fig. 6(a)]. Such temperature behavior of $\rho(T)$ is reminiscent of the one reported for $Lu_2Ir_3Si_5$, where a thermal hysteresis of 40 K is observed [29], and is a hallmark of a first-order structural phase transition. For the canonical CDW system $Er_5Ir_4Si_{10}$ [30] the electrical resistivity is characterized by the absence of a thermal hysteresis. However, a CDW scenario for $Th_3Ir_4Ge_{13}$ cannot be completely excluded taking into account the predisposition of the 3 : 4 : 13 structures to structural modulation [21].

The resistivity of $U_3Ir_4Ge_{13}$ in the temperature range 1.9–4.5 K fits to $\rho_0 + A_{FL}T^2$ [inset to Fig. 6(b)] with a residual resistivity $\rho_0 = 6.97$ $\mu\Omega$ m from impurity scattering, and the cross section of the quasiparticle-quasiparticle scattering $A_{FL} = 1.34 \times 10^{-2}$ $\mu\Omega$ m K$^{-2}$. The Kadowaki-Woods ratio [31] $R_{KW} = A_{FL}/\gamma^2 = 1.0 \times 10^{-5}$ $\mu\Omega$ cm K$^{-2}$(mol K$^2$ mJ$^{-1}$)$^2$ for $U_3Ir_4Ge_{13}$ is the same as reported for Fermi liquids and thus metallic systems. In the second derivative $d^2\rho/dT^2$ a broad weak anomaly at ≈20 K [not shown in Fig. 6(b)] corresponding to the ferromagnetic ordering is observed. With increasing temperature $\rho(T)$ of $U_3Ir_4Ge_{13}$ passes through a broad maximum centered at ≈250 K and then decreases (a small drop of the resistivity observed at ∼50 K is an artifact). Such behavior is reminiscent of that observed for U-containing intermetallic compounds with high $p$-element content such as, e.g., UAuSi [32], $UCu_5Al$, [33], and $U_{1.2}Fe_4Si_{9.7}$ [34], the former two are also considered as Kondo systems. Since the electrical resistivity of $Th_3Ir_4Ge_{13}$ is affected by a first-order phase transition we cannot take a closer look at the U 5$f$-electron contribution to the resistivity of $U_3Ir_4Ge_{13}$ and make conclusions on the possible Kondo behavior of this compound.

### E. Specific heat

The low-temperature specific heat of $Th_3Ir_4Ge_{13}$ is given in Fig. 7. For $T < 6$ K it is described by $\gamma T + \beta T^3 + \delta T^5$, where $\gamma$ is the Sommerfeld coefficient of the electronic specific heat, and $\beta$ and $\delta$ are the first terms of the harmonic lattice approximation for the phonon contribution. A fit results in $\gamma = 4.72(3)$ mJ mol$^{-1}$ K$^{-2}$, $\beta = 1.41(3)$ mJ mol$^{-1}$ K$^{-4}$,

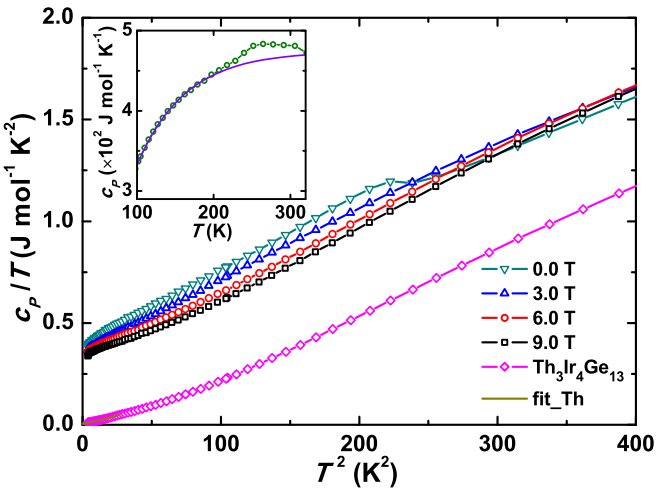


FIG. 7. (Color online) Specific heat of $U_3Ir_4Ge_{13}$ vs temperature near the ferromagnetic transition in different magnetic fields and of $Th_3Ir_4Ge_{13}$. The (red) line shows the fit (see text). Inset: High-temperature specific heat of $Th_3Ir_4Ge_{13}$ (circles) near the $T_k$ together with an estimated background (line).

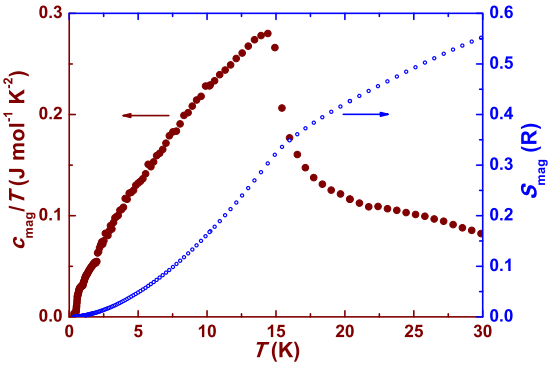


FIG. 8. (Color online) Temperature dependence of the specific heat of $U_3Ir_4Ge_{13}$ after subtraction of phonon reference ($Th_3Ir_4Ge_{13}$) and $\gamma_{mag}$ in $c_{mag}/T(T)$ representation (brown scales) together with magnetic entropy (blue scales).

which is equivalent to a Debye temperature $\Theta_D = 302$ K, and $\delta = 7.06(5) \times 10^{-3}$ mJ mol$^{-1}$ K$^{-6}$. The small value of $\gamma$ indicates a low DOS at the Fermi level of ≈2.0 states eV$^{-1}$ f.u.$^{-1}$ and metallic properties of $Th_3Ir_4Ge_{13}$ being well in agreement with the band-structure calculations (see Sec. III G). In the temperature range 220–320 K the specific heat of $Th_3Ir_4Ge_{13}$ shows a broad anomaly (inset to Fig. 7). The "jump" $\Delta c_p$ centered at ≈240 K is ≈30 J mol$^{-1}$ K$^{-1}$. It is comparable with the jumps observed in typical CDW compounds such as $Er_5Ir_4Si_{10}$ ($\Delta c_p = 160$ J mol$^{-1}$ K$^{-1}$) [30] or $Lu_5Ir_4Si_{10}$ ($\Delta c_p = 160$ J mol$^{-1}$ K$^{-1}$) [35]. Latent heat could not be detected at the phase transition, which is partially due to used experimental method and setup. For low temperatures, $Th_3Ir_4Ge_{13}$ is considered as phonon reference for $U_3Ir_4Ge_{13}$ taking into account the close structural relationship, and the almost identical molar masses and unit cell volume.

The specific heat of $U_3Ir_4Ge_{13}$ in various magnetic fields is shown in Fig. 7. A clear anomaly, associated with the ferromagnetic ordering, is observed at $T_C = 15.2$ K in zero field. The specific heat of $U_3Ir_4Ge_{13}$ consists also of, besides electronic and phonon parts, a magnetic contribution $c_{mag}(T)$. To obtain the electronic $c_{el}$ part the $c_P$ of $Th_3Ir_4Ge_{13}$ was subtracted from $c_P(T)$ of $U_3Ir_4Ge_{13}$. This results in a $5f$ related electronic term $\gamma_f = 320(2)$ mJ mol$^{-1}$ K$^{-2}$ at 0.35 K. The magnetic contribution $c_{mag}$ (Fig. 8) was obtained by further subtraction of the obtained $\gamma_f$. The integration of $c_{mag}(T)/T$ yields the magnetic entropy $S_{mag} \approx 0.42R\ln 2$ at the transition temperature (Fig. 8). The value is very similar to those observed for ferromagnetic U-containing compounds as, for instance, UPtAl ($T_C = 43$ K, $S_{mag} \approx 0.71R\ln 2$) [36], UIrAl ($T_C = 62$ K, $S_{mag} \approx 0.33R\ln 2$) [37], or URhSi ($T_C = 10.1$ K, $S_{mag} \approx 0.17R\ln 2$) [38]. The small values of magnetic entropy and the large $\gamma_f$ suggest the predominant itinerant nature of the U moments. However, the shortest U-U distance of 4.473(1) Å in the structure of $U_3Ir_4Ge_{13}$ is considerably larger than these observed in the case of the above listed 1 : 1 : 1 compounds with $d_{(U\text{-}U)} < 3.7$ Å and thus is well above the Hill limit, which amounts $d_{(U\text{-}U)} = 3.5$ Å [39]. From this point of view the nature of U $5f$ states in $U_3Ir_4Ge_{13}$ can be phenomenologically considered to be at least partially itinerant.

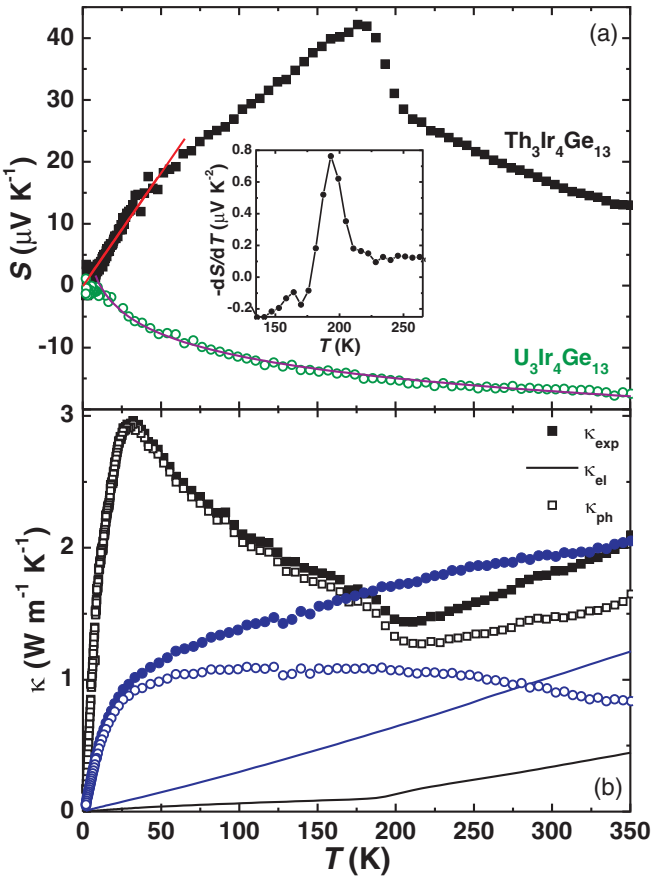


FIG. 9. (Color online) (a) Thermopower $S$ vs $T$ for $Th_3Ir_4Ge_{13}$ and $U_3Ir_4Ge_{13}$ together with the fits (see text). Inset: $-dS/dT$ of $Th_3Ir_4Ge_{13}$ vs $T$. (b) Temperature dependence of the thermal conductivity $\kappa(T)$ of $Th_3Ir_4Ge_{13}$(■) and $U_3Ir_4Ge_{13}$(●), with their electronic ($\kappa_{el}$, continuous line) and phonon ($\kappa_{ph}$, □ and ◯) contributions.

### F. Thermal transport

The temperature dependence of the Seebeck coefficient $S(T)$ of the thermopower of $Th_3Ir_4Ge_{13}$ is presented in Fig. 9. It is positive in the whole studied temperature range implying the dominance of the hole-type carriers. In the range $1.8 < T < 50$ K it is well fitted to $S = \alpha T$ with $\alpha = 0.36\ \mu$V K$^{-2}$. In a one-band model with an energy-independent relaxation time $\alpha$ is estimated as $\pi^2 k_B^2/2eE_F$. The value $E_F = 0.1$ eV, obtained from this formula is lower than usually observed for systems with metallic behavior (e.g., $E_F = 0.72$ eV for $LaAgSb_2$ [40]). The dimensionless parameter $q = N_A e\alpha/\gamma_{exp}$ (Faraday constant $N_A e \approx 96\,485$ C mol$^{-1}$), which characterizes the thermoelectric material in terms of an effective charge carrier concentration per f.u. (or the Fermi volume $V_F$ of the charge carriers) [41], is estimated to be 7.4, which is larger than $q \sim 1$ expected for Fermi liquids.

With further increasing temperature $S(T)$ of $Th_3Ir_4Ge_{13}$ increases and than shows a sudden drop after which it decreases further. The maximum in $-dS/dT$ at ≈193 K [inset to Fig. 9(a)] coincides with $T_k^{cool} = 194$ K obtained from $-d\rho/dT$ [$S(T)$ is measured in cooling, too]. The Seebeck coefficient is a sensitive probe for changes in the DOS (e.g., for CDW ordering, structural phase transitions, and any gap

formation on the Fermi surface) [29,40,42]. Interestingly, in typical CDW compounds as $Lu_5Ir_4Si_{10}$ [42] or $Lu_2Ir_3Si_5$ [29] the discontinuity in $S(T)$ at the transition temperature is 2–3 $\mu$V K$^{-1}$, while in the present case it is $\approx 14$ $\mu$V K$^{-1}$, which suggests larger changes at $E_F$ and represents thus most probably a first-order structural phase transition.

The Seebeck coefficient $S(T)$ of $U_3Ir_4Ge_{13}$ decreases in the whole studied temperature range [Fig. 9(a)]. This decrease shows logarithmical character for $T < 25$ K [inset, Fig. 9(a)]. The negative value of the Seebeck coefficient of $U_3Ir_4Ge_{13}$ implies predominant electron-type carriers. At room temperature the Seebeck coefficient is 16.6 $\mu$V K$^{-1}$, which is in the range ~10–15 $\mu$V K$^{-1}$ expected for normal actinide intermetallic compounds in absence of many-body effects [43]. Interestingly, no anomaly is visible in $S(T)$ and $\kappa(T)$ of $U_3Ir_4Ge_{13}$ at the temperature of ferromagnetic ordering ($T_C = 15$ K). This can be explained by the small ordered magnetic moments and low magnetic entropy involved in this transition.

The thermal conductivity $\kappa(T)$ for $Th_3Ir_4Ge_{13}$ and $U_3Ir_4Ge_{13}$ is presented in Fig. 9(b). Both compounds show low thermal conductivity, which is comparable with that observed for cage compounds (e.g., filled skutterudites) [44,45]. $\kappa(T)$ may be decomposed into electronic $\kappa_{el}$ and phonon $\kappa_{ph}$ contributions. $\kappa_{el}$ is calculated from the Wiedemann-Franz law $\kappa_{el}(T) = L_0 T/\rho(T)$, where $L_0$ is the Lorenz number $2.44 \times 10^{-8}$ W $\Omega$ K$^{-2}$ and the phonon contribution $\kappa_{ph}$ is estimated by subtracting $\kappa_{el}$ from the measured $\kappa$. For $Th_3Ir_4Ge_{13}$, $\kappa(T)$ decreases with decreasing temperature down to 200 K showing a minimum in agreement with the presence of the first-order phase transition. Interestingly, the electronic contribution to the thermal conductivity at the transition is negligible. With further decreasing temperature $\kappa(T)$ of $Th_3Ir_4Ge_{13}$ increases, passes through a maximum at ≈30 K and rapidly drops following roughly a linear law for $T < 5$ K.

No anomalies were observed in the thermal conductivity of $U_3Ir_4Ge_{13}$. It decreases smoothly with decreasing temperature down to 50 K and then rapidly drops down towards smaller values. The phonon contribution $\kappa_{ph}$ of $U_3Ir_4Ge_{13}$ at 300 K is very low; $\kappa_{ph}^{300K} = 0.9$ W m$^{-1}$ K$^{-1}$, and it is of the same order of magnitude as for such well known thermoelectrics as $(Bi/Sb)_2Te_3$ ($\kappa_{ph}^{300K} = 0.6$ W m$^{-1}$ K$^{-1}$) [46] or $Yb_{14}Mn_{1-x}Al_xSb_{11}$ ($\kappa_{ph}^{300K} = 0.55$ W m$^{-1}$ K$^{-1}$) [47]. The dimensionless figure of merit of $U_3Ir_4Ge_{13}$ as a thermoelectric material is negligible ($ZT = 0.006$ at 300 K).

### G. Electronic structure

The optimized electronic structure of idealized $Th_3Ir_4Ge_{13}$, assuming $Yb_3Rh_4Sn_{13}$ type [1], is presented in Fig. 10. The obtained DOS is reminiscent of those reported for thorium [48,49], rare-earth [50], and alkaline-earth [51] containing platinum germanium filled skutterudites and $\{Ca,Y,Yb\}_3Pt_4Ge_{13}$ [11,13] compounds and shows almost the same features. The separate DOS structure in the energy range between −13 and −7 eV is mostly due to the mixing of the Ge2 4*s* and Ir 5*d* states. The broad valence band extending from −6 eV upon to the Fermi level ($E_F$) is due to hybridization of Ge2 4*p*, Ir 5*d*, and Th 6*d* states. The Fermi level is situated in a spike of the DOS with $N(E_F) = 4.87$ states eV$^{-1}$ f.u.$^{-1}$,

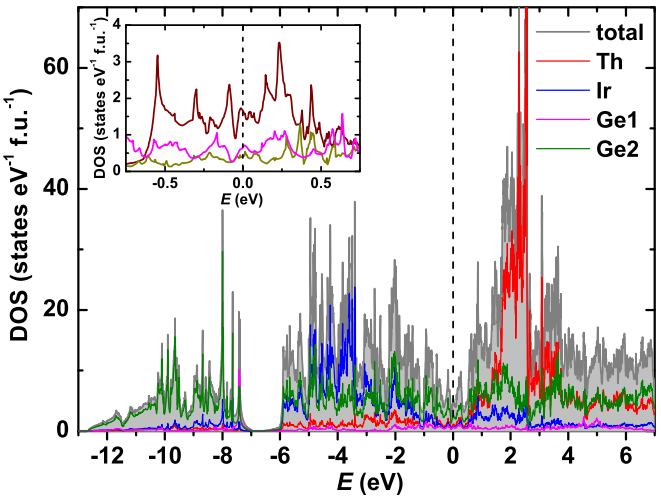


FIG. 10. (Color online) Calculated electronic density of states (DOS) for the idealized $Th_3Ir_4Ge_{13}$ structure. The Fermi level is indicated by the dashed line. Inset: Ge1 partial DOS in the close vicinity to the Fermi level for different interatomic Ge1-Ge2 distances: $d_{Ge1\text{-}Ge2} = 3.324$ Å (brown line), $d_{Ge1\text{-}Ge2} = 3.062$ Å (magenta line), and $d_{Ge1\text{-}Ge2} = 2.551$ Å (dark yellow line).

which would correspond to $\gamma^{theor} = 11.5$ mJ mol$^{-1}$ K$^{-2}$ in disagreement with the experimentally observed value of 4.72(3) mJ mol$^{-1}$ K$^{-2}$. These findings indicate instability of the idealized $Th_3Ir_4Ge_{13}$ structure. The Fermi level is mostly populated by the Ge1 4*p* (0.62 states eV$^{-1}$ f.u.$^{-1}$), Ge2 4*p* (2.15 states eV$^{-1}$ f.u.$^{-1}$), and Th 6*d* and 5*f* (≈ 1.1 states eV$^{-1}$ f.u.$^{-1}$). Calculations assuming different lengths of Ge1-Ge2 contacts in the structure of $Th_3Ir_4Ge_{13}$ have been performed. As one can see from the inset to Fig. 10, the shortening of this distance from 3.324 to 3.062 Å leads to the separation of the Ge1 4*p* into bonding and antibonding states and thus to a remarkable reduction of the DOS at $E_F$. Further shrinking of $d_{Ge1\text{-}Ge2}$ does not affect the DOS. Also, changes of the Ge1-Ge2 distance do not influence the Ge2 4*p* states. Thus, only changes in the bonding situation between Ge1 centering the icosahedra and the Ge2-atoms from the framework, caused by the strong reduction of the symmetry (e.g., $\{Ca,Y,Yb\}_3Pt_4Ge_{13}$ [11,13]) or by the splitting of Ge2 site, as observed in the crystal structure of $Th_3Ir_4Ge_{13}$ (which cannot be simulated theoretically) are leading to low DOS and the appearance of a dip at $E_F$. The broad maximum above $E_F$ is due to the Th 5*f*, 6*d*, and 7*s* states, which are unoccupied. This suggests transfer of these electrons towards the Ir-Ge framework in the idealized $Th_3Ir_4Ge_{13}$ structure.

The electronic structure of $U_3Ir_4Ge_{13}$ calculated within LSDA + $U$ approach is given in Fig. 11. It shows nearly the same features as described above for idealized $Th_3Ir_4Ge_{13}$: the separate DOS (−13 to −7.5 eV) due to the mixing of the Ge 4*s* and Ir 5*d* states; the broad valence band (−6 to 0 eV) due to the hybridization of Ge 4*p*, Ir 5*d*, and U 5*f* states in the close vicinity to the $E_F$. The Fermi level is mostly populated by U 5*f* spin up states [2.65 states eV$^{-1}$ f.u.$^{-1}$ of $N(E_F) = 5.15$ states eV$^{-1}$ f.u.$^{-1}$] (inset to Fig. 11). The number of 5*f* electrons estimated from the band-structure calculation is 2.92 which would indicate a configuration close to U $5f^3$ for $U_3Ir_4Ge_{13}$.

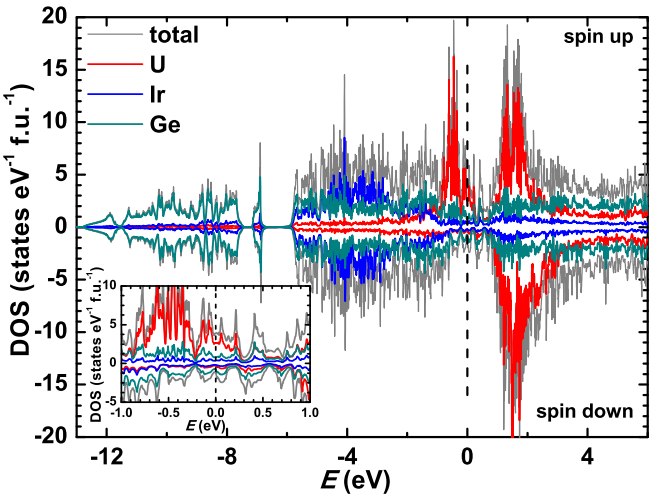


FIG. 11. (Color online) Calculated electronic density of states (DOS) within the LSDA + $U$ ($U = 2$ eV) approach for the rhombohedral $U_3Ir_4Ge_{13}$ structure. The Fermi level is indicated by the dashed line.

A similar number of 5$f$ electrons (i.e., 2.89) [52] is calculated theoretically and confirmed by high-energy-resolution core-level and valence-band photoelectron spectroscopic studies for $UFeGa_5$ – a compound with itinerant nature of 5$f$ states and enlarged U-U contacts ($d_{U\text{-}U2} = 4.26$ Å) [53]. The electronic structure of $UFeGa_5$ is also characterized by a hybridization of Fe 6$d$ and U 5$f$ states in the close vicinity to $E_F$, similar as it is observed for $U_3Ir_4Ge_{13}$ (hybridization of Ir 5$d$ and U 5$f$). All these findings are in line with the observed prevalent itinerant character of U 5$f$ electrons in $U_3Ir_4Ge_{13}$.

The band-structure calculations result also in a ferromagnetic ground state for $U_3Ir_4Ge_{13}$ with a magnetic moment of 2.33 $\mu_B$ per formula unit, which is in fair agreement with experimentally observed value of 1.76 $\mu_B$ f.u.$^{-1}$. A possible explanation for this discrepancy could be the reduction of the ordered moment by sizable spin fluctuations not included in the framework of LSDA.

## IV. CONCLUSIONS

$Th_3Ir_4Ge_{13}$ crystallizes with primitive cubic $Tm_3Co_4Ge_{13}$ type of structure, where the 24$k$ Wyckoff position occupied by Ge2 is split. This leads to the appearance of bonding contacts (Ge1-Ge2$_1$) between Ge atoms centering icosahedra and these from the framework. $U_3Ir_4Ge_{13}$ shows the noncentrosymmetric rhombohedral structural arrangement observed for HT-$Y_3Pt_4Ge_{13}$ type. Both structures are derivatives of the well known primitive cubic prototype $Yb_3Rh_4Sn_{13}$. Theoretical calculations within LDA approach clearly indicate the instability of the ideal structural arrangement observed in the $Yb_3Rh_4Sn_{13}$ prototype for the $Th_3Ir_4Ge_{13}$ compound. XANES performed at the U $M_4$ edge indicates an oxidation state of uranium close to +4 for uranium in $U_3Ir_4Ge_{13}$.

Sharp anomalies at ≈200 K are observed in the magnetic susceptibility, electrical resistivity, specific heat, thermopower, and thermal conductivity of $Th_3Ir_4Ge_{13}$. From the jump of the magnetic susceptibility $|\Delta\chi_0|$ a small reduction of the DOS by ∼0.4 eV$^{-1}$ f.u.$^{-1}$ was deduced. This value as well as the jump in the specific heat $\Delta c_p \approx 30$ J mol$^{-1}$ K$^{-1}$ are reminiscent of the effects observed for typical CDW systems. However, the fact that the electrical resistivity of the warming and cooling runs at the transition temperatures for $Th_3Ir_4Ge_{13}$ do not coincide as well as a large drop of ≈14 $\mu$V K$^{-1}$ in the thermopower would rather indicate a first-order structural phase transition. Finally, to shed light on the structural changes in $Th_3Ir_4Ge_{13}$, temperature dependent high-resolution x-ray diffraction experiments on high quality single crystals have to be performed. All our attempts to prepare single crystals suitable for such a study failed until now.

$U_3Ir_4Ge_{13}$ is a ferromagnet with $T_C = 15$ K, effective magnetic moment $\mu_{eff}$ of 4.19 $\mu_B$ f.u.$^{-1}$ and coercive field ≈0.3 T at 1.8 K. The small value of magnetic entropy $S_{mag} \approx 0.58R\ln 2$, deduced from the specific heat at the ordering temperature, the absence of large effects at $T_C$ in the thermopower and the thermal conductivity, as well as the strong contribution of U 5$f$ partial DOS at the Fermi Level in the electronic structure suggest a predominantly itinerant nature of the uranium 5$f$ states. The decrease of the electrical resistivity of $U_3Ir_4Ge_{13}$ with increasing temperature as well as the reduced jump in specific heat at $T_C$ and small magnetic entropy of the transition (also reported for some typical Ce- and Yb-containing Kondo lattices, e.g., $CePd_2Ge_2$, $YbAuCu_4$, etc.) [54] hint to a possible Kondo scenario. However, since the uranium 5$f$-electrons contribution to the resistivity could not be separated, this statement requires an additional confirmation. Interestingly, the phonon contribution to the thermal conductivity of $U_3Ir_4Ge_{13}$ at 300 K is of the same order of magnitude as some well known thermoelectrics, nonetheless, the efficiency of $U_3Ir_4Ge_{13}$ as a thermoelectric material is negligible.

## ACKNOWLEDGMENTS

The authors thank H. Borrmann and U. Burkhardt for help during x-ray diffraction and EDXS experiments and L. Akselrud for fruitful discussions.

[1] J. Remeika, G. Espinosa, A. Cooper, H. Barz, J. Rowell, D. McWhan, J. Vandenberg, D. Moncton, Z. Fisk, L. Woolf *et al.*, Solid State Commun. **34**, 923 (1980).

[2] P. Villars, *Pearson's Handbook, Crystallographic Data for Intermetallic Phases* (ASM International, Materials Park, OH, 1997).

[3] K. Wang and C. Petrovic, Phys. Rev. B **86**, 024522 (2012).

[4] C. N. Kuo, H. F. Liu, C. S. Lue, L. M. Wang, C. C. Chen, and Y. K. Kuo, Phys. Rev. B **89**, 094520 (2014).

[5] L. E. Klintberg, S. K. Goh, P. L. Alireza, P. J. Saines, D. A. Tompsett, P. W. Logg, J. Yang, B. Chen, K. Yoshimura, and F. M. Grosche, Phys. Rev. Lett. **109**, 237008 (2012).

[6] D. A. Tompsett, Phys. Rev. B **89**, 075117 (2014).
[7] S. K. Goh, D. A. Tompsett, P. J. Saines, H. C. Chang, T. Matsumoto, M. Imai, K. Yoshimura, and F. M. Grosche, Phys. Rev. Lett. **114**, 097002 (2015).
[8] B. Lloret, B. Chevalier, P. Gravereau, B. Darriet, and J. Etourneau, J. Phys. Colloques **49**, C8-487 (1988).
[9] G. Espinosa, A. Cooper, and H. Barz, Mater. Res. Bull. **17**, 963 (1982).
[10] F. Mirambet, B. Chevalier, L. Fournes, M. Besnus, P. Gravereau, and J. Etourneau, J. Magn. Magn. Mater. **118**, 187 (1993).
[11] R. Gumeniuk, L. Akselrud, K. O. Kvashnina, W. Schnelle, A. A. Tsirlin, C. Curfs, H. Rosner, M. Schöneich, U. Burkhardt, U. Schwarz *et al.*, Dalton Trans. **41**, 6299 (2012).
[12] R. Gumeniuk, M. Schöneich, K. O. Kvashnina, L. Akselrud, A. A. Tsirlin, M. Nicklas, W. Schnelle, O. Janson, Q. Zheng, C. Curfs *et al.*, Dalton Trans. **44**, 5638 (2015).
[13] R. Gumeniuk, M. Nicklas, L. Akselrud, W. Schnelle, U. Schwarz, A. A. Tsirlin, A. Leithe-Jasper, and Y. Grin, Phys. Rev. B **87**, 224502 (2013).
[14] A. Leithe-Jasper, H. Borrmann, and W. Hönle, *Max Plank Institute for Chemical Physics of Solids, Scientific Report* (Dresden, 2003–2005), p. 25.
[15] STOE Powder Software, WinXPow (version 2), Darmstadt, STOE and Cie GmbH, 2001.
[16] L. Akselrud and Y. Grin, J. Appl. Crystallogr. **47**, 803 (2014).
[17] C. Gauthier, V. A. Solé, R. Signorato, J. Goulon, and E. Moguiline, J. Synchrotron Rad. **6**, 164 (1999).
[18] P. Glatzel, T.-C. Weng, K. Kvashnina, J. Swarbrick, M. Sikora, E. Gallo, N. Smolentsev, and R. A. Mori, J. Electron Spectrosc. Relat. Phenom. **188**, 17 (2013).
[19] K. Koepernik and H. Eschrig, Phys. Rev. B **59**, 1743 (1999).
[20] J. P. Perdew and Y. Wang, Phys. Rev. B **45**, 13244 (1992).
[21] L. Akselrud and V. Davydov, Visnyk Lviv. Univ. Ser. Khim. **39**, 112 (2001).
[22] J. Emsley, *The Elements* (Clarendon Press, Oxford, 1998).
[23] K. O. Kvashnina, S. M. Butorin, P. Martin, and P. Glatzel, Phys. Rev. Lett. **111**, 253002 (2013).
[24] C. Booth, Y. Jiang, D. Wang, J. Mitchell, P. Tobash, E. Bauer, M. Wall, P. Allen, D. Sokaras, D. Nordlund *et al.*, PNAS **109**, 10205 (2012).
[25] M. Continentino, Eur. Phys. J. B **13**, 31 (2000).
[26] Y. Nagano, N. Araoka, A. Mitsuda, H. Yayama, H. Wada, M. Ichihara, M. Isobe, and Y. Ueda, J. Phys. Soc. Jpn. **82**, 064715 (2013).
[27] N. Mott and H. Jones, *The Theory of the Properties of Metals and Alloys* (Dover, New York, 1958).
[28] E. Gopal, *Specific Heat at Low Temperatures* (Plenum, New York, 1966).
[29] Y. K. Kuo, K. M. Sivakumar, T. H. Su, and C. S. Lue, Phys. Rev. B **74**, 045115 (2006).
[30] F. Galli, S. Ramakrishnan, T. Taniguchi, G. J. Nieuwenhuys, J. A. Mydosh, S. Geupel, J. Lüdecke, and S. van Smaalen, Phys. Rev. Lett. **85**, 158 (2000).
[31] K. Kadowaki and S. Woods, Solid State Commun. **58**, 507 (1986).
[32] V. Tran and R. Troć, J. Phys. B: Condens. Matter **186–188**, 744 (1993).
[33] R. Troć, R. Andruszkiewicz, R. Pietri, and B. Andraka, J. Magn. Magn. Mater. **183**, 132 (1998).
[34] S. Noguchi, K. Okuda, T. Adachi, Y. Haga, E. Yamamoto, and Y. Ōnuki, J. Phys. Soc. Jpn. **66**, 2572 (1997).
[35] S. Ramakrishnan and J. Mydosh, J. Magn. Magn. Mater. **310**, 207 (2007).
[36] A. V. Andreev, M. Diviš, P. Javorský, K. Prokeš, V. Sechovský, J. Kuneš, and Y. Shiokawa, Phys. Rev. B **64**, 144408 (2001).
[37] A. Andreev, N. Mushnikov, F. Honda, V. Sechovský, P. Javorský, and T. Goto, J. Magn. Magn. Mater. **272–276**, E337 (2004).
[38] K. Prokeš, T. Wand, A. Andreev, M. Meissner, F. Honda, and V. Sechovský, J. Alloys Compd. **460**, 47 (2008).
[39] H. Hill, in *Plutonium and Other Actinides*, edited by W. Miner (Met. Soc. AIME, New York, 1970), p. 2.
[40] C. S. Lue, Y. F. Tao, K. M. Sivakumar, and Y. K. Kuo, J. Phys.: Condens. Matter **19**, 406230 (2007).
[41] V. Zlatić, R. Monnier, J. K.Freericks, and K. W. Becker, Phys. Rev. B **76**, 085122 (2007).
[42] Y.-K. Kuo, C. S. Lue, F. H. Hsu, H. H. Li, and H. D. Yang, Phys. Rev. B **64**, 125124 (2001).
[43] R. Troć, Z. Bukowski, C. Sułkowski, H. Misiorek, J. A. Morkowski, A. Szajek, and G. Chełkowska, Phys. Rev. B **70**, 184443 (2004).
[44] C. Uher, Semicond. Semimet. **69**, 139 (2001).
[45] B. C. Sales, D. Mandrus, B. C. Chakoumakos, V. Keppens, and J. R. Thompson, Phys. Rev. B **56**, 15081 (1997).
[46] B. Poudel, Q. Hao, Y. Ma, Y. Lan, A. Minnich, B. Yu, X. Yan, D. Wang, A. Muto, D. Vashaee *et al.*, Science **320**, 634 (2008).
[47] C. A. Cox, E. S. Toberer, A. A. Levchenko, S. R. Brown, G. J. Snyder, A. Navrotsky, and S. M. Kauzlarich, Chem. Mater. **21**, 1354 (2009).
[48] V. H. Tran, D. Kaczorowski, W. Miiller, and A. Jezierski, Phys. Rev. B **79**, 054520 (2009).
[49] E. Bauer, X.-Q. Chen, P. Rogl, G. Hilscher, H. Michor, E. Royanian, R. Podloucky, G. Giester, O. Sologub, and A. P. Goncalves, Phys. Rev. B **78**, 064516 (2008).
[50] R. Gumeniuk, W. Schnelle, H. Rosner, M. Nicklas, A. Leithe-Jasper, and Y. Grin, Phys. Rev. Lett. **100**, 017002 (2008).
[51] H. Rosner, J. Gegner, D. Regesch, W. Schnelle, R. Gumeniuk, A. Leithe-Jasper, H. Fujiwara, T. Haupricht, T. C. Koethe, H.-H. Hsieh *et al.*, Phys. Rev. B **80**, 075114 (2009).
[52] S.-i. Fujimori, T. Ohkochi, I. Kawasaki, A. Yasui, Y. Takeda, T. Okane, Y. Saitoh, A. Fujimori, H. Yamagami, Y. Haga *et al.*, J. Phys. Soc. Jpn. **81**, 014703 (2012).
[53] Y. Grin, P. Rogl, and K. Hiebl, J. Less Comm. Met. **121**, 497 (1986).
[54] M. Besnus, A. Braghta, N. Hamdaoui, and A. Meyer, J. Magn. Magn. Mater. **104–107**, 1385 (1992).